ACS APPLIED MATERIALS & INTERFACES

Letter

www.acsami.org

Band Gap Tuning of $CH_3NH_3Pb(Br_{1-x}Cl_x)_3$ Hybrid Perovskite for Blue Electroluminescence

Naresh K. Kumawat,[†] Amrita Dey,[†] Aravindh Kumar,[‡] Sreelekha P. Gopinathan,[§] K. L. Narasimhan,[‡] and Dinesh Kabra*[,†]

[†]Department of Physics, [‡]Department of Electrical Engineering, and [§]Centre for Research in Nanotechnology & Science (CRNTS), Indian Institute of Technology Bombay, Powai, Mumbai, India 400076

Supporting Information

ABSTRACT: We report on the structural, morphological and optical properties of $AB(Br_{1-x}Cl_x)_3$ (where, A = $CH_3NH_3^+$, B = Pb^{2+} and x = 0 to 1) perovskite semiconductor and their successful demonstration in green and blue emissive perovskite light emitting diodes at room temperature. The bandgap of perovskite thin film is tuned from 2.42 to 3.16 eV. The onset of optical absorption is dominated by excitonic effects. The coulomb field of the exciton influences the absorption at the band edge. Hence, it is necessary to explicitly account for the enhancement of the absorption through the Sommerfield factor. This enables us to correctly extract the exciton binding energy and the electronic bandgap. We also show that the lattice constant varies linearly with the fractional chlorine content satisfying Vegards law.

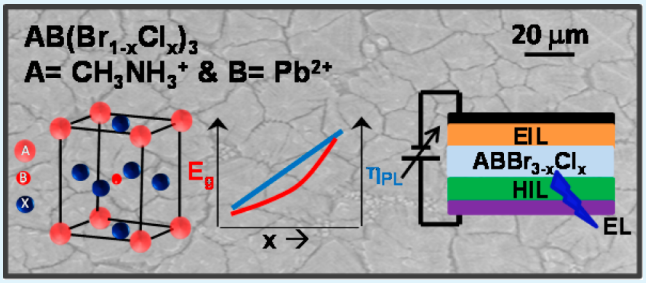

KEYWORDS: *perovskite, bandgap tuning, Bowing parameter, Urbach energy, Sommerfield factor, Blue-PeLED*

In recent years, organic lead halide (ABX_3 = where A = $CH_3NH_3^+$, B divalent ion Pb^{2+} and X is halide ion) based perovskites have emerged as an important optoelectronic material. In a very short time span perovskite thin film based solar cell have shown impressively high efficiency (>18%) by many groups which has ignited the attention of researchers in this area throughout the world.[1−9] More recently, we and others have shown high performance visible (green and red) and IR emissive perovskite light emitting diodes (PeLED).[10−13] The low-temperature solution processability and the completely tunable optical direct bandgap over a wide range makes it a potential candidate for both tandem solar cells, light emitting diodes and tunable laser over the visible range.[9−11,14−16] An exact knowledge of electronic levels are a prerequisite to make a good optoelectronic device and for understanding the device physics.[17,18] There are very few results that discuss in great detail the role of excitonic states in these materials, though these wide bandgap perovskites solar cells have >10% solar cell efficiency.[19] Hence, understanding of the structural and optical properties of wider bandgap perovskites is significantly important to develop high performance optoelectronic devices and provided the motivation for the work reported in this paper.

In this paper, we report on the detailed structural, morphological and optical properties of a wide range of mixed chloride-bromide perovskite ($AB(Br_{1-x}Cl_x)_3$) systems with band gap ranging from 2.42 to 3.16 eV. We present measurements of the energy gap and the lattice constant as a function of the alloy composition and also demonstrate first preliminary $J-V-L$ characteristics and EL spectra of blue color PeLED. Material synthesis and experimental details are given in the Supporting Information.

STRUCTURAL AND MORPHOLOGICAL PROPERTIES

Figure 1a, b show the crystal structure and XRD diffraction peaks of $AB(Br_{1-x}Cl_x)_3$ (where A = $CH_3NH_3^+$, B divalent metal ion (Pb^{2+}) perovskite on glass/PEDOT:PSS. As seen in Figure 1 a, the divalent metal is at the center, A is at the cube corner position and halide (Br/Cl) atoms at the face centered position.[20−22] In literature, pure $ABBr_3$ and $ABCl_3$ have cubic crystal structure at room temperature with 5.95 and 5.66 Å lattice parameters, respectively.[23] From XRD pattern we have observed that mixed perovskite $AB(Br_{1-x}Cl_x)_3$ is crystalline. We see from Figure 1b, that the diffraction peak shifts toward higher angle (2θ) with increase in chloride concentration. The X-ray diffraction peak positions for the different compositions are summarized in Table 1 and Table S1 in the Supporting Information. Because both $ABBr_3$ and $ABCl_3$ perovskite have cubic crystal structure, it is reasonable to expect that $AB(Br_{1-x}Cl_x)_3$ perovskite should also exist in the same structure.[24,25] This we will discuss later. Figure 1c shows the FESEM morphology image of a mixed perovskite sample

Received: March 11, 2015
Accepted: June 8, 2015
Published: June 8, 2015

DOI: 10.1021/acsami.5b02159
ACS Appl. Mater. Interfaces 2015, 7, 13119−13124

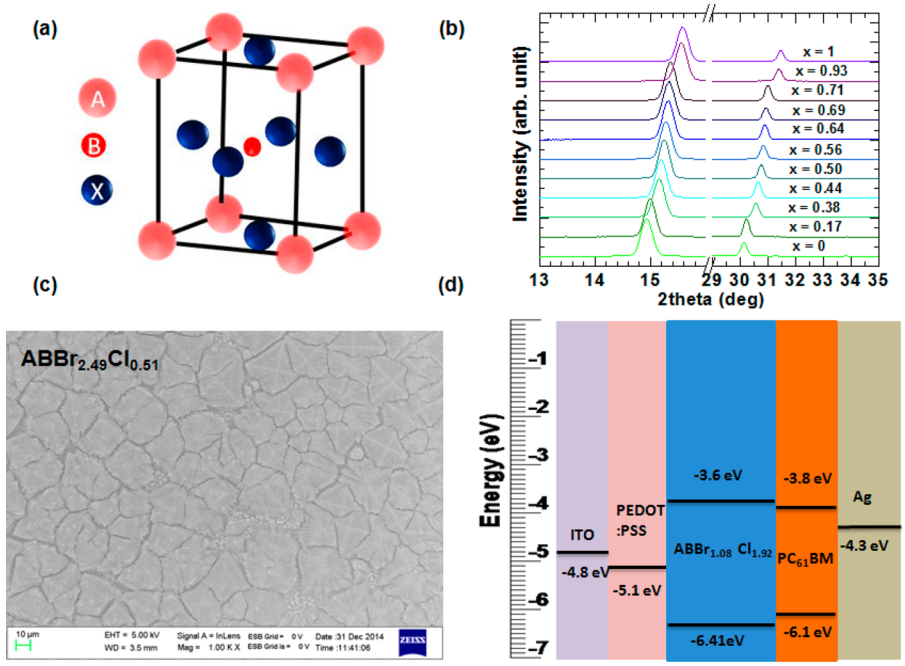

Figure 1. Structural and morphological studies: (a) Typical crystal structure of organometallic halide (ABX_3) where A is for $CH_3NH_3^+$, B is for divalent metal ion (Pb^{2+}) and X is for halide ion. (b) XRD pattern for annealed film of $AB(Br_{1-x}Cl_x)_3$ (x = 0 to 1) perovskite materials on glass/PEDOT:PSS substrate. (c) FESEM image of $ABBr_{2.49}Cl_{0.51}$ perovskite film on ITO/PEDOT:PSS substrate. (d) Electroluminescent diodes structure based on $ABBr_{1.08}Cl_{1.92}$, energy level values are taken from literature.[10,17]

Table 1. Lattice Parameter and XRD First-Order 2θ Peak Position of $AB(Br_{1-x}Cl_x)_3$ Perovskite Film for x = 0 to 1 Deposited on Glass/PEDOT:PSS

perovskite	lattice parameter (Å)	1st order 2θ peak (deg)
$ABBr_3$	5.95	14.93
$ABBr_{2.49}Cl_{0.51}$	5.90	14.99
$ABBr_{1.86}Cl_{1.14}$	5.83	15.15
$ABBr_{1.68}Cl_{1.32}$	5.82	15.19
$ABBr_{1.5}Cl_{1.5}$	5.80	15.24
$ABBr_{1.32}Cl_{1.68}$	5.78	15.27
$ABBr_{1.08}Cl_{1.92}$	5.76	15.31
$ABBr_{0.93}Cl_{2.07}$	5.75	15.32
$ABBr_{0.87}Cl_{2.13}$	5.74	15.35
$ABBr_{0.21}Cl_{2.79}$	5.68	15.55
$ABCl_3$	5.66	15.57

deposited on PEDOT:PSS-coated ITO substrates after annealing. Here the coverage of $AB(Br_{1-x}Cl_x)_3$ perovskite is reasonably uniform with crystal domain sizes of about 10−20 μm. Substitution of Cl with Br significantly influences the domain size of perovskite (Figure S1 in the Supporting Information). The composition of the mixed halide is determined using energy dispersive X-ray analysis (EDX) mode of FESEM.The film composition is mentioned in the morphology image of each perovskite film in Figure 1c and Figure S1 in the Supporting Information. Figure 1d shows the energy level diagram corresponding to $ABBr_{1.08}Cl_{1.92}$ composition. Here we assume that the conduction band level is fixed and with chloride concentration the valence bond level goes deeper.[17]

OPTICAL PROPERTIES

Figure 2a shows the optical absorption of the mixed perovskite alloy films $AB(Br_{1-x}Cl_x)_3$ (x = 0 to 1) for different alloy compositions. The absorption consists of three broad features; a sub band gap absorption tail at low energy followed by a strong exciton peak and then by band-to-band transitions. As expected, the onset of absorption moves to higher energy with increasing chlorine concentration suggesting that the band gap increases with increasing chlorine fraction. The band gap of a direct band gap semiconductor is estimated using the relation

$$(\alpha E)^2 = A(E - E_g) \quad (1)$$

where E is the photon energy and α is the measured absorption coefficient. However, we see from the absorption spectrum (Figure 2a) that the optical absorption in the vicinity of the band gap is enhanced due to the exciton absorption. The use of eq 1 to obtain the band gap is invalid when exciton absorption dominates the absorption spectrum near the band gap of the semiconductor and can be understood as follows.[26] The exciton energy levels are given by a Rydberg series,[26] $E_n^{ex} = E_g - R_y^*/n^2$ where E_g is the band gap, R_y^* the exciton Rydberg constant, and n is an integer. As n increases, the exciton lines become closer in energy and at the band edge the absorption coefficient becomes large and constant, instead of being zero, as in the case when excitons do not dominate the absorption spectrum.[26] This is the reason for the nonapplicability of eq 1 near to $E = E_g$.

The enhancement of the absorption coefficient by taking into account for the coulomb field of the exciton is known as the Sommerfeld factor ($S(\varepsilon)$) and needs to be explicitly taken into account for determination of the band gap. ε is a dimensionless quantity related to photon energy E by $\varepsilon = (E - E_g)/R_y^*$, with E_g being the effective bandgap. We have calculated the band gap for the different alloy samples by evaluating the Sommerfeld factor for excitons in a 3D system.[27,28]

The absorption coefficient ($\alpha(\varepsilon)$) is given by the following expression

DOI: 10.1021/acsami.5b02159
ACS Appl. Mater. Interfaces 2015, 7, 13119−13124

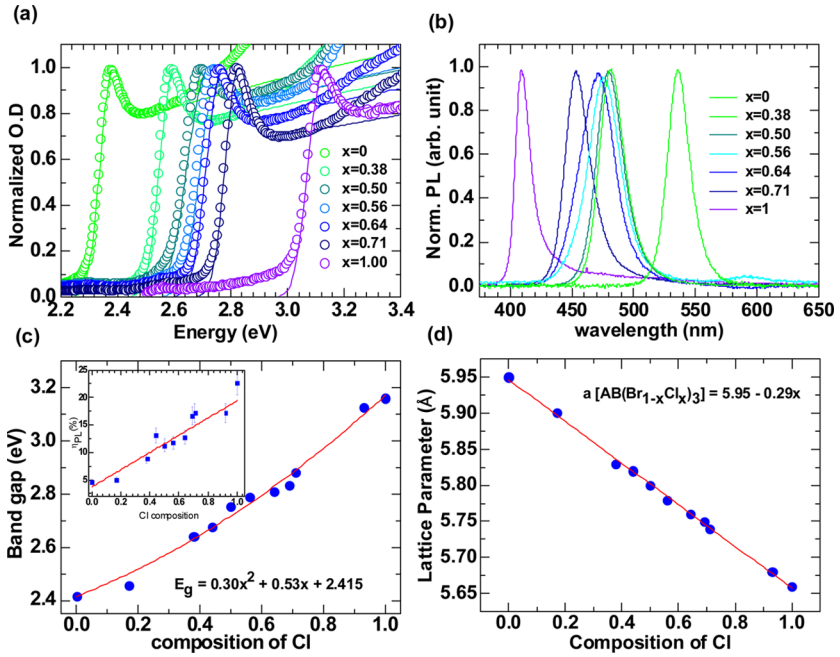

Figure 2. Optical properties of perovskites: (a) UV−vis absorbance spectra on energy scale for $AB(Br_{1-x}Cl_x)_3$ perovskite, where x varies from 0 to 1. (b) Photoluminescence spectra of $AB(Br_{1-x}Cl_x)_3$ perovskite semiconductor film prepared on quartz substrates with excitation wavelength corresponds to their UV−vis spectra. (c)The quadratic behavior of band gap of $AB(Br_{1-x}Cl_x)_3$ perovskite with chloride content (d) Lattice parameter of $AB(Br_{1-x}Cl_x)_3$perovskite as a function of chlorine content.

Table 2. Various Photo-physical Parameters Associated with Absorption and Emission of $AB(Br_{1-x}Cl_x)_3$ Perovskite Film for x = 0 to 1

Cl composition	band gap (eV)	exciton peak (eV)	fwhm Exciton peak (meV)	exciton BE (meV)	Urbach energy (meV)	PL peak (eV)	fwhm PL peak (meV)
0	2.42	2.37	88	45	38	2.31	89
0.17	2.46	2.41	92	45	38	2.35	96
0.38	2.64	2.59	98	54	39	2.55	107
0.44	2.68	2.63	92	53	39	2.58	125
0.50	2.75	2.69	138	61	45	2.59	141
0.56	2.79	2.74	126	55	49	2.61	185
0.64	2.81	2.75	108	57	44	2.63	185
0.69	2.84	2.78	100	58	44	2.67	128
0.71	2.88	2.82	96	62	45	2.74	148
0.93	3.13	3.06	90	62	42	2.97	146
1	3.16	3.11	102	64	43	3.03	106

$$\alpha(\varepsilon) = \frac{A_0}{2\pi^2 R_y^* a_o^{*3}} \frac{2}{\Gamma}\sqrt{\frac{\ln 2}{\pi}} \left\{ \sum_{n=1}^{\infty} \frac{4\pi}{n^3} \exp\left[-4\ln 2 \frac{\left(\varepsilon + \frac{1}{n^2}\right)^2}{\Gamma^2} \right] + \int_0^{\infty} \exp\left[-4\ln 2 \frac{(\varepsilon' - \varepsilon)^2}{\Gamma^2} \right] \sqrt{\varepsilon'}\, S(\varepsilon') d\varepsilon' \right\} \quad (2)$$

$$S(\varepsilon) = \frac{2\pi/\sqrt{\varepsilon}}{1 - \exp[-2\pi/\sqrt{\varepsilon}]} \quad (3)$$

$$R_y^* = \frac{\mu_r e^4}{2h^2(4\pi\varepsilon_0 k)^2} \quad (4)$$

$$a_0^* = \frac{4\pi\varepsilon h^2}{\mu_r e^2} \quad (5)$$

where A_0 is a costant proportional to the oscillator strength, Γ is the full-width at half-maximum of the excitonic peak divided by R^*_y. a_0* is the Bohr radius of exciton, μ_r is the reduced mass, ε_0 is vacuum permittivity, κ is the relative dielectric constant, and h is the Planck's constant.

In eq 2, the sum in the first term is due to the sum over all the exciton transitions and the second term is due to the band-to-band transitions including the Sommerfeld factor. The exciton peak is taken to be a Gaussian (inhomogeneous broadening) with a width of Γ- the width arising due to disorder. The solid line in Figure 2a and Figure S2c in the Supporting Information shows the fit for the absorption spectrum for $AB(Br_{1-x}Cl_x)_3$ perovskite films. Figure S2a, b in the Supporting Information shows the deconvolution of the absorption spectra for the exciton and band-to-band transitions, respectively. Table 2 shows the calculated band gaps and

DOI: 10.1021/acsami.5b02159
ACS Appl. Mater. Interfaces 2015, 7, 13119−13124

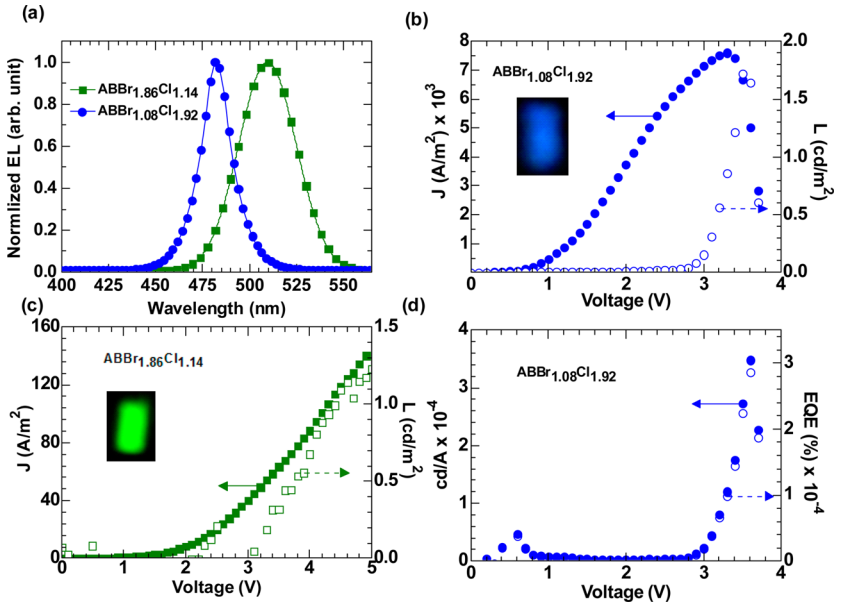

Figure 3. Electroluminescent diodes: (a) EL spectra of blue and green PeLEDs for $ABBr_{1.08}Cl_{1.92}$ and $ABBr_{1.86}Cl_{1.14}$ perovskite, respectively. *J*−*V*−*L* characteristics of (b) ITO/PEDOT:PSS/$ABBr_{1.08}Cl_{1.92}$/$PC_{61}BM$/Ag- (blue) and (c) ITO/PEDOT:PSS/$ABBr_{1.86}Cl_{1.14}$/$PC_{61}BM$/Ag (green)-based PeLEDs with insets of operational PeLED picture. (d) EQE vs biasing voltage for blue and green PeLEDs, derived from *J*−*V*−*L* curve and EL spectra.

exciton binding energy for the different compositions reported here. The band gap varies from 2.42 eV ($ABBr_3$) to 3.16 eV ($ABCl_3$). The exciton binding energy remains reasonably constant between ∼50−60 meV over the whole composition range. The exciton binding energy E_x is given by[26,27]

$$E_x = (\mu_r q^4)/(2h^2\varepsilon_0{}^2k^2/4\pi^2) = (\mu_r/k^2)13.6 \text{ eV} \quad (6)$$

A constant binding energy implies that (μ_r/κ^2) is constant over the whole composition range. There are no reliable values for μ_r and κ reported for the mixed chlorine-bromine perovskites. If we assume the effective mass to be that of the free electron mass, using eq 6 κ is estimated to be about 16.5, which is close to recently measured for $ABI_{3-x}Cl_x$ ($\kappa \approx 18$) case using capacitance measurement.[29]

We now briefly comment on the broadening of the exciton peak. Figure S3 in the Supporting Information is a plot of ln (α) vs *E*. The low energy side of the absorption consists of two parts, a region where the absorption follows a relation $\alpha = \exp(E/E_u)$ and at lower energy there is an excess absorption. We interpret the exponential absorption as an Urbach tail and the Urbach energy E_u as a measure of the disorder. The excess absorption at low energy is defect absorption arising due to grain boundary defects and other traps in the material.[26,30] Table 2 also shows the Urbach energy for the samples. The Urbach energy varies between 38 and 45 meV and to first order is independent of the alloy composition. This suggests that the disorder in the films is dominated by structural disorder and not by compositional disorder.

Figure 2b and Figure S2d in the Supporting Information shows photoluminescence spectra of $AB(Br_{1-x}Cl_x)_3 (x = 0 \text{ to } 1)$ after annealing. Table 2 shows the position of the PL peak for the all these samples. The PL peak should coincide with the exciton peak energy in the absence of disorder. In the presence of disorder, the excited carriers can thermaliz to lower energy sites causing the PL peak position to be slightly red-shifted with the exciton absorption peak position.[31] We see from the data in Table 2 that the PL peak is red-shifted by 40−100 meV with respect to the exciton peak position. The larger shift qualitatively correlates with the larger Gaussian peak width. The inset in Figure 2c shows the PL efficiency of forward emission vs Cl composition in $AB(Br_{1-x}Cl_x)_3$ these films.[10,32] PL efficiency of these films shows an almost linear increase from ∼5% (at $x = 0$) to ∼25% (at $x = 1$) with increased composition of Cl ion as substitution of Br ion. It is expected that phonon assisted nonradative decay channels (phonon collisional decay rate α $1/\Delta E$) become increasingly less important as the band gap increases resulting in a higher PL yield.[33] The exact nature of this behavior is not very clear at this stage; however, it is a useful property for lasing and EL devices.[10,11,34,35]

Figure 2c shows the band gap vs Chloride composition (x = 0−1) and can be written as[36]

$$E_g[AB(Br_{1-x}Cl_x)_3] = xE_g(ABCl_3) + (1-x)E_g(ABBr_3) - x(1-x)b \quad (7)$$

where x is chloride composition and b is a bowing parameter. Value of b is obtained using least-squares fitting (red line) of data in Figure 2c by a second order polynomial that gives the following quadratic equation:

$$E_g = 0.30x^2 + 0.53x + 2.42 \quad (8)$$

From eqs 7 and 8, we find the bowing parameter to be b = 0.30 eV. This number is significantly smaller as compare to inorganic semiconductors and also relatively smaller when compared with $AB(I_{3-x}Br_x)_3$ (b = 0.33) perovskite.[24,37−39] Using this relation, it is possible to obtain the alloy composition from a measurement of the band gap of the material. Smaller value of bowing parameter, in general, suggests that alloy disorder and degree of fluctuation in the crystal field is less.[40]

Figure 2d shows lattice parameter vs halide composition.The lattice parameter varies linearly with x, where x defines the fractional composition of the chlorine in the alloy and satisfies

DOI: 10.1021/acsami.5b02159
ACS Appl. Mater. Interfaces 2015, 7, 13119−13124

Vegard's law. The lattice parameter for any fraction x is given by $a[AB(Br_{1-x}Cl_x)_3] = xa(ABCl_3) + (1 - x)a(ABBr_3)$, where $a[AB(Br_{1-x}\ Cl_x)_3]$, $a(ABCl_3)$, and $a(ABBr_3)$ are the lattice parameters for the mixed halide and pure phase of chloride and bromide perovskites, respectively. The lattice parameter decreases with increasing chlorine content as the chlorine ionic radius is lower than that for bromine.[41] Using the data of Figure 2d, it is now possible to estimate the alloy composition from a measurement of the lattice parameter.

ELECTROLUMINISCENCE STUDIES

Now, we present preliminary results for green and blue electroluminescence using the mixed perovskites. The device structure for PeLEDs is shown in Figure 1d. Figure 3a shows steady state electroluminescence (EL) spectra of ITO/PEDOT:PSS/$ABBr_{1.08}Cl_{1.92}$ /$PC_{61}BM$/Ag and ITO/PEDOT:PSS/$ABBr_{1.86}Cl_{1.14}$ /$PC_{61}BM$/Ag diode. EL peaks are observed at 482 and 510 nm, respectively. The EL peak (482 and 510 nm) is red-shifted with respect to the PL peak (471 and 486 nm, Figure 2b). This small redshift of EL peak with respect to PL can be due to interplay of charge carrier vs exciton dynamics. The red-shift of EL might be related to thermalization of injected carriers to lower energy sites during transport through the film. Figure 3b, c shows the $J-V-L$ characteristics of a blue and a green PeLED. The insets in the figures show the image of the operational PeLEDs. Figure 3d shows external quantum efficiency (EQE) for blue ($ABBr_{1.08}Cl_{1.92}$) and green ($ABBr_{1.86}Cl_{1.14}$) PeLEDs (corresponding luminance efficiency (cd/A) for blue and green PeLED are in Figure S5 in the Supporting Information). These results suggest that though PL efficiency is high for $ABBr_{1.08}Cl_{1.92}$ as compared to $ABBr_{1.86}Cl_{1.14}$ perovskite film, however, charge carrier balance in $ABBr_{1.08}Cl_{1.92}$ is significantly poorer (injection barrier for holes) than $ABBr_{1.86}Cl_{1.14}$ which results in lower EL EQE (EQE = $\gamma\eta_{PL}\eta_{out\text{-}coupling}$ where γ = charge carrier balance, η_{PL} = PL yield and $\eta_{out\text{-}coupling}$ = out-coupling efficiency).[42]

The current density numbers for blue emissive PeLED is almost an order higher than the current in the green emissive PeLED. We expect that this is due to poor charge confinement and relatively poor morphology of $ABBr_{1.08}Cl_{1.92}$ as compared to $ABBr_{1.86}Cl_{1.14}$ (Figure 1d, Figure S1b, d in the Supporting Information). Efficiency of these PeLEDs are on lower side for this device structure, as charge injection is much more challenging as compared to low band gap perovskites of the same family. Use of optimal charge injection layers will significantly increase the efficiency of these devices. Studies on optimal charge injection layers for blue emissive PeLEDs are currently underway..

In conclusion, we have studied the structural, morphological and optical properties of bromine-chlorine $AB(Br_{1-x}Cl_x)_3$(x = 0 to 1) mixed-halide perovskites. The optical absorption spectrum is dominated by excitons at energy close to the band edge. This results in an enhancement of the optical absorption coefficient at the optical band edge. Hence extraction of the band gap using the relation $(\alpha E)^2 = A(E - E_g)$ is invalid. The correct value for the band gap has to take into account the Sommerfield factor taking into account both exciton absorption and band-to-band transitions. This procedure enables a proper extraction of both the band gap and the exciton binding energy. The exciton binding energy is almost independent of alloy composition and is about 50−60 meV. The absorption coefficient of the low energy edge of the exciton absorption increases exponentially with energy reminiscent of an Urbach tail.The Urbach energy is independent of the alloy composition. We hence conclude that the disorder potential is related to structural defects and not dominated by alloy disorder.

Using the values of the band gap, we have evaluated the bowing parameter of the optical gap with alloy concentration. This is a very useful result as a correct measurement of the band gap allows an independent estimate of the alloy concentration using the bowing parameter. We show that the lattice constant follows Vegard's law for these systems. This allows material composition to be also estimated from a measurement of the lattice constant. The photoluminescence emission energy is red-shifted with respect to the exciton peak—presumably a consequence of disorder. The quantum efficiency of luminescence increases with increase in band gap, suggesting that non radiative pathways are less efficient in large band gap materials. On the basis of our results, we also present preliminary results of blue and green EL devices.

ASSOCIATED CONTENT

Supporting Information

Material synthesis and methods, Figures S1−S6, Table S1, and relevant references.The Supporting Information is available free of charge on the ACS Publications website at DOI: 10.1021/acsami.5b02159.

AUTHOR INFORMATION

Corresponding Author

*E-mail: dkabra@iitb.ac.in.

Notes

The authors declare no competing financial interest.

ACKNOWLEDGMENTS

This work is partially supported by the IITB Seed grant (12IRCCSG044). We also acknowledge support of Center of Excellence in Nanoelectronics (CEN) for device fabrication facility and National Center for Photovoltaic Research and Education (NCPRE) for characterization of morphology. We thank Prof. Anil Kumar from Chem. IITB-Mumbai for providing synthesis facility and Dr. Sandip Ghosh (TIFR) for useful discussions on optical properties. A.D. acknowledges UGC for a research fellowship.

REFERENCES

(1) Liu, M.; Johnston, M. B.; Snaith, H. J. Efficient Planar Heterojunction Perovskite Solar Cells by Vapour Deposition. *Nature* **2013**, *501*, 395−398.

(2) Burschka, J.; Pellet, N.; Moon, S.-J.; Humphry-Baker, R.; Gao, P.; Nazeeruddin, M. K.; Gratzel, M. Sequential Deposition as a Route to High-Performance Perovskite-Sensitized Solar Cells. *Nature* **2013**, *499*, 316−319.

(3) Green, M. A.; Ho-Baillie, A.; Snaith, H. J. The Emergence of Perovskite Solar Cells. *Nat. Photonics* **2014**, *8*, 506−214.

(4) Snaith, H. J. Perovskites: The Emergence of a New Era for Low-Cost, High-Efficiency Solar Cells. *J. Phys. Chem. Lett.* **2013**, *4*, 3623−3630.

(5) Kim, H.-S.; Im, S. H.; Park, N.-G. Organolead Halide Perovskite: New Horizons in Solar Cell Research. *J. Phys. Chem. C* **2014**, *118*, 5615−5625.

(6) Agarwal, S.; Seetharaman, M.; Kumawat, N. K.; Subbiah, A. S.; Sarkar, S. K.; Kabra, D.; Namboothiry, M. A. G.; Nair, P. R. On the Uniqueness of Ideality Factor and Voltage Exponent of Perovskite-Based Solar Cells. *J. Phys. Chem. Lett.* **2014**, *5*, 4115−4121.

DOI: 10.1021/acsami.5b02159
ACS Appl. Mater. Interfaces 2015, 7, 13119−13124

(7) Hodes, G.; Cahen, D. Photovoltaics: Perovskite Cells Roll Forward. *Nat. Photonics* **2014**, *8*, 87−88.
(8) Zhou, H.; Chen, Q.; Li, G.; Luo, S.; Song, T.-B.; Duan, H.-S.; Hong, Z.; You, J.; Liu, Y.; Yang, Y. Interface Engineering of Highly Efficient Perovskite Solar Cells. *Science* **2014**, *345*, 542−546.
(9) Sutherland, B. R.; Hoogland, S.; Adachi, M. M.; Kanjanaboos, P.; Wong, C. T. O.; McDowell, J. J.; Xu, J.; Voznyy, O.; Ning, Z.; Houtepen, A. J.; Sargent, E. H. Perovskite Thin Films via Atomic Layer Deposition. *Adv. Mater.* **2015**, *27*, 53−58.
(10) Kumawat, N. K.; Dey, A.; Narasimhan, K. L.; Kabra, D. Near Infrared to Visible Electroluminescent Diodes Based on Organometallic Halide Perovskites: Structural and Optical Investigation. *ACS Photonics* **2015**, *2* (3), 349−354.
(11) Tan, Z.-K.; Moghaddam, R. S.; Lai, M. L.; Docampo, P.; Higler, R.; Deschler, F.; Price, M.; Sadhanala, A.; Pazos, L. M.; Credgington, D.; Hanusch, F.; Bein, T.; Snaith, H. J.; Friend, R. H. Bright Light-Emitting Diodes based on Organometal Halide Perovskite. *Nat. Nanotechnol.* **2014**, *9*, 687−692.
(12) Kim, Y.-H.; Cho, H.; Heo, J. H.; Kim, T.-S.; Myoung, N.; Lee, C.-L.; Im, S. H.; Lee, T.-W. Multicoloured Organic/Inorganic Hybrid Perovskite Light-Emitting Diodes. *Adv. Mater.* **2014**, *27*, 1248−1254.
(13) Wetzelaer, G.- J. A. H.; Scheepers, M.; Sempere, A. M.; Momblona, C.; Avila, J.; Bolink, H. J. Trap-Assisted Non-radiative Recombination in Organic−Inorganic Perovskite Solar Cells. *Adv. Mater.* **2015**, *27*, 1837−1841.
(14) Deschler, F.; Price, M.; Pathak, S.; Klintberg, L. E.; Jarausch, D.-D.; Higler, R.; Huttner, S.; Leijtens, T.; Stranks, S. D.; Snaith, H. J.; Atature, M.; Phillips, R. T.; Friend, R. H. High Photoluminescence Efficiency and Optically Pumped Lasing in Solution-Processed Mixed Halide Perovskite Semiconductors. *J. Phys. Chem. Lett.* **2014**, *5*, 1421−1426.
(15) Xing, G.; Mathews, N.; Lim, S. S.; Yantara, N.; Liu, X.; Sabba, D.; Gratzel, M.; Mhaisalkar, S.; Sum, T. C. Low-Temperature Solution-Processed Wavelength-Tuneable Perovskites for Lasing. *Nat. Mater.* **2014**, *13*, 476−480.
(16) Chen, K.; Barker, A. J.; Morgan, F. L. C.; Halpert, J. E.; Hodgkiss, J. M. Effect of Carrier Thermalization Dynamics on Light Emission and Amplification in Organometal Halide Perovskites. *J. Phys. Chem. Lett.* **2015**, *6*, 153−158.
(17) Schulz, P.; Edri, E.; Kirmayer, S.; Hodes, G.; Cahen, D.; Kahn, A. Interface Energetics in Organo-Metal Halide Perovskite−Based Photovoltaic Cells. *Energy Environ. Sci.* **2014**, *7*, 1377−1381.
(18) Kabra, D.; Lu, L. P.; Song, M. H.; Snaith, H. J.; Friend, R. H. Efficient Single-Layer Polymer Light-Emitting Diodes. *Adv. Mater.* **2010**, *22*, 3194−3198.
(19) Heo, J. H.; Song, D. H.; Im, S. H. Planar $CH_3NH_3PbBr_3$ Hybrid Solar Cells with 10.4% Power Conversion Efficiency, Fabricated by Controlled Crystallization in the Spin-Coating Process. *Adv. Mater.* **2014**, *26*, 8179−8183.
(20) Zhang, M.; Lyu, M.; Yu, H.; Yun, J.-H.; Wang, Q.; Wang, L. Stable and Low-Cost Mesoscopic $CH_3NH_3PbI_2Br$ Perovskite Solar Cells by using a Thin Poly(3-hexylthiophene) Layer as a Hole Transporter. *Chem.—Eur. J.* **2015**, *21*, 434−439.
(21) Yin, W.-J.; Yang, J.-H.; Kang, J.; Yanb, Y.; Wei, S. H. Halide Perovskite Materials for Solar Cells: A Theoretical Review. *J. Mater. Chem. A* **2015**, DOI: 10.1039/c4ta05033a.
(22) Baikie, T.; Fang, Y.; Kadro, J. M.; Schreyer, M.; Wei, F.; Mhaisalkar, S. G.; Graetzeld, M.; White, T. J. Synthesis and Crystal Chemistry of the Hybrid Perovskite $(CH_3NH_3)PbI_3$ for Solid-State Sensitised Solar Cell Applications. *J. Mater. Chem. A* **2013**, *1*, 5628−5641.
(23) Chia, L.; Swainsona, I.; Cranswicka, L.; Herb, J.-H.; Stephensb, P.; Knop, O. The Ordered Phase of Methylammonium Lead Chloride $CH_3ND_3PbCl_3$. *J. Solid State Chem.* **2005**, *178*, 1376−1385.
(24) Noh, J. H.; Im, S. H.; Heo, J. H.; Mandal, T. N.; Seok, S. I. Chemical Management for Colorful, Efficient, and Stable Inorganic−Organic Hybrid Nanostructured Solar Cells. *Nano Lett.* **2013**, *13*, 1764−1769.
(25) Chen, W.-T.; Saito, T.; Hayashi, N.; Takano, M.; Shimakawa, Y. Ligand-Hole Localization in Oxides with Unusual Valence Fe. *Sci. Rep.* **2012**, *2*, 449−455.
(26) Yu, P. Y.; Cardona, M. *Fundamentals of Semiconductors Physics and Materials Properties*, 4th ed.; Springer: Heidelberg, Germany, 2010.
(27) Chuang, S. L. *Physics of Optoelectronics Devices*, 1st ed.; Wiley: New York, 1995.
(28) Mukherjee, A.; Ghosh, S. Origin of additional Spectral features in Modulated Reflectance Spectra of 2-Dimensional Semiconductor Systems. *J. Appl. Phys.* **2014**, *115*, 123503.
(29) Samiee, M.; Konduri, S.; Ganapathy, B.; Kottokkaran, R.; Abbas, H. A.; Kitahara, A.; Joshi, P.; Zhang, L.; Noack, M.; Dalal, V. Defect Density and Dielectric Constant in Perovskite Solar Cells. *Appl. Phys. Lett.* **2014**, *105*, 153502.
(30) Venkateshvaran, D.; Nikolka, M.; Sadhanala, A.; Lemaur, V.; Zelazny, M.; Kepa, M.; Hurhangee, M.; Kronemeijer, A. J.; Pecunia, V.; Nasrallah, J.; Romanov, I.; Broch, K.; McCulloch, I.; Emin, D.; Olivier, Y.; Cornil, J.; Beljonne, D.; Sirringhaus, H. Approaching Disorder-free Transport in High-Mobility Conjugated Polymers. *Nature* **2014**, *515*, 384−388.
(31) Hirano, D.; Tayagaki, T.; Kanemitsu, Y. Disorder-induced Rapid Localization of Electron-hole Plasmas in Highly excited $InxGa_{1-x}N$ Mixed Crystals. *Phys. Rev. B* **2008**, *77*, 073201−073204.
(32) Lee, X. Y.; Wu, C.; Verma, A. K.; Ranganathan, R.; Yablonovitch, E. Non-Destructive Testing By Absolute Room Temperature Photoluminescence Quantum Efficiency of GaAs Solar Cell. *Conference Record of the Twenty Fifth IEEE Photovoltaic Specialists Conference*; New York, May 13−17, 1996 ; IEEE: Piscataway, NJ, 1996; pp 141−142.
(33) Silfvast, W. T. *Laser Fundamentals*, 2nd ed.; Cambridge University Press: Cambridge, U.K., 2003.
(34) Lu, L. P.; Kabra, D.; Friend, R. H. Barium Hydroxide as an Interlayer Between Zinc Oxide and a Luminescent Conjugated Polymer for Light-Emitting Diodes. *Adv. Funct. Mater.* **2012**, *22*, 4165−4171.
(35) Song, M. H.; Kabra, D.; Wenger, B.; Friend, R. H.; Snaith, H. J. Optically-Pumped Lasing in Hybrid Organic−Inorganic Light-Emitting Diodes. *Adv. Funct. Mater.* **2009**, *19*, 2130−2136.
(36) Wang, M.; Fei, G. T.; Zhang, Y. G.; Kong, M. G.; Zhang, L. D. Tunable and Predetermined Bandgap Emission in Alloyed ZnS_xSe_{1-x} Nanowires. *Adv. Mater.* **2007**, *19*, 4491−4494.
(37) El-Shazly, A. A.; El-Naby, M. M. H.; Kenawy, M. A.; El-Nahass, M. M.; El-Shair, H. T.; Ebrahim, A. M. Optical Properties of Ternary ZnS_xSe_{1-x} Polycrystalline Thin Films. *Appl. Phys. A: Mater. Sci. Process* **1985**, *36*, 51−53.
(38) Sharma, T. K.; Jangir, R.; Porwal, S.; Kumar, R.; Ganguli, T.; Zorn, M.; Zeimer, U.; Bugge, F.; Weyers, M.; Oak, S. M. Compositional Dependence of the Bowing Parameter for Highly Strained InGaAs/GaAs Quantum Wells. *Phys. Rev. B* **2009**, *80*, 165403.
(39) Venugopal, R.; Lin, P.-I; Chen, Y.-T. Photoluminescence and Raman Scattering from Catalytically Grown $Zn_xCd_{1-x}Se$ Alloy Nanowires. *J. Phys. Chem. B* **2006**, *110*, 11691−11696.
(40) Hill, R. Energy-Gap Variations in Semiconductor Alloys. *J. Phys. C: Solid State Phys.* **1974**, *7*, 521−526.
(41) Kuo, Y.-K.; Liou, B.-T.; Yen, S.-H.; Chu, H.-Y. Vegard's Law Deviation in Lattice constant and Band Gap Bowing parameter of Zincblende $In_xGa1_{-x}N$. *Opt. Commun.* **2004**, *237*, 363−369.
(42) Kabra, D.; Friend, R. H. Efficiency beyond Spin-Statistics in Polymer-Based Hybrid LEDs. *Optoelectron. Commun., SPIE* **2014**, DOI: 10.1117/2.1201409.005542.

NOTE ADDED AFTER ASAP PUBLICATION

This paper was published on the Web on June 11, 2015, with minor errors in equation 2. The corrected version was reposted on the same day.

DOI: 10.1021/acsami.5b02159
ACS Appl. Mater. Interfaces 2015, 7, 13119−13124